1   Utilization of APC residues from sewage sludge incineration process as activator of alkali-
2   activated slag/glass powder material

3

4   Keke Sun, Hafiz Asad Ali, Dongxing Xuan, Jiaxing Ban, Chi Sun Poon[*]

5

6   Department of Civil and Environmental Engineering, The Hong Kong Polytechnic University,
7   Hung Hom, Kowloon, Hong Kong, China

8

9   Corresponding author: cecspoon@polyu.edu.hk

10

11   **Abstract:** In this paper, the soluble salts from the air pollution control (APC) residues of a sewage
12   sludge incinerator and solid sodium silicate were used as a hybrid activator to prepare alkali-
13   activated materials (AAMs) using slag and waste glass powder (GP) as the precursors. The effect
14   of the hybrid activator on the mechanical properties and its reaction mechanism was discussed. The
15   experimental results showed that the APC residues obviously decreased the early compressive
16   strength of the AAMs due to its lower activity, but a steady growth of later compressive strength
17   was achieved due to the dense microstructure. The alkali-activated slag and GP/slag suffered from
18   severe drying shrinkage, but the drying shrinkage of the AAMs reduced by 30%~50% when the
19   20% APC residues were added. In addition, when the APC residues and GP was used, the
20   insufficient aluminum and calcium contents restrained the formation of the C-(A)-S-H gels in the
21   alkali-activated GP/slag, and the N-(C)-A-S-H gels were formed until the available Ca was
22   exhausted. Some crystalline materials including the ettringite, hydrotalcite, albite and Friedel's
23   salts were detected in the alkali-activated slag/GP after the incorporation of the APC residues in
24   addition to the N-S-H gels.

25

26   **Keywords:** Alkali activated materials; Waste glass powder; Slag; APC residues; Drying
27   shrinkage.

28

29   **1.   Introduction**
30   It has been acknowledged that alkali-activated materials (AAMs) can be designed to achieve
31   excellent mechanical characteristics and durability with a low carbon footprint. Such
32   environmental-friendly materials can be produced using various industrial by-products or waste
33   materials as precursors [1-3]. The precursors usually require highly alkaline solutions such as
34   sodium hydroxide and sodium silicate solution (or water glass) for their activation [4]. These strong

35 and corrosive alkaline solutions are necessary to obtain high pH environment for precursor
36 dissolution and strength development. But this results in an undesirable rapid setting, high
37 shrinkage and consequently microcracks, and problems with efflorescence [5-7]. In addition, the
38 on-site production of AAMs is still limited by its fast setting and lack of suitable retarders [8].

39 Waste incineration is an efficient technique used to treat dewatered sewage sludge with its
40 significant advantages for reducing the volume and mass as well as energy recovery [9]. However,
41 air pollution control (APC) residues, a by-product of this technology, still requires a new recycling
42 route. Depending on the characteristics of sewage sludge that it is treating, the APC residues may
43 contain high levels of chlorides, sulfates and heavy metals [10, 11]. The high chloride and sulfates
44 contents are most due to the use of seawater in wastewater flushing in a city such as Hong Kong
45 [12]. The previous studies [13] also confirmed that the risk of heavy metals leaching from the APC
46 residues of the sewage sludge incinerator in Hong Kong was relatively low because of the stringent
47 control of industrial effluent in the city.

48 Several studies reported the physical properties of the AAMs produced and the reaction
49 mechanism of sulfate-activated slag. Cristelo et al. developed a one-part geopolymer from fly ash
50 and slag activated by the Na_2SO_4 and NaCl [14]. The results showed that the Na_2SO_4 had a positive
51 effect on the mechanical properties of alkali-activated fly ash/slag since it accelerated the
52 precipitation of ettringite as a secondary reaction product, but the presence of NaCl delayed the
53 reaction rate and setting time. The Na_2SO_4 manufacturing uses a lower amount of energy compared
54 with that of waterglass and sodium hydroxide [15-17]. But the compressive strength of Na_2SO_4-
55 activated slag was lower than those using sodium hydroxide and waterglass as the activator.
56 Therefore, it seems that the APC residues can be utilized as an activator to formulate AAMs.
57 Lampris et al. [18] reported that slag can be successfully activated by adding 50 wt.% APC residues
58 and attained a compressive strength of 20.6 MPa. Ren et al. [19] found that using the washed
59 municipal solid waste incineration fly ash with rich sulfate as an activator for the slag was harmless
60 to the environment, and the formation of ettringite was responsible for the early compressive
61 strength development. Therefore, the rich sodium sulfate from the APC residues can be utilised as
62 activator for slag binder, but the effect of using the APC residues with sodium silicate as a hybrid
63 activator to formulate AAM and their reaction mechanisms have not been studied previously.

64 The precursor of AAMs should be available locally to reduce the transportation cost, industrial
65 wastes, and environmental impacts. In Hong Kong, waste glass contributes to a high percentage of
66 the municipal solid waste stream, and its recycling rate was less than 20%. Recently, waste glass
67 powder has been investigated as a possible precursor to produce the AAMs [20-22]. A significant
68 strength reduction of the alkali-activated waste glass powder was reported as compared to using

69 slag as the precursor. The combined use of glass powder and slag could provide Ca and Al sources

70 to form the stable C-(N)-A-S-H gel and compensate for the strength loss [23]. In addition, adding

71 glass powder would reduce the water loss of the alkali-activated metakaolin under drying condition,

72 leading to a low drying shrinkage [24]. Zhang et al., developed a novel way to incorporate waste

73 glass cullet and glass powder into AAMs, and the drying shrinkage level could be controlled to less

74 than $1000\mu\varepsilon$ [25]. Therefore, as a potential alkali-siliceous material, the waste glass powder can be

75 used as raw materials to improve the physical properties of the AAMs.

76 To maximize the recycling of waste glass and APC residues, this study aimed to explore the

77 potential of using the APC residues with solid sodium silicate as a hybrid activator to produce one-

78 part AAMs using slag and glass powder as the precursors. The effect of the APC residues on the

79 compressive strength and drying shrinkage of the alkali-activated slag/glass powder mortar were

80 evaluated. Meanwhile, the reaction products in the alkali-activated slag/glass powders were

81 characterized by the X-ray diffraction (XRD), heat evolution, nuclear magnetic resonance (NMR),

82 and SEM tests.

83

84 **2. Experimental program**

85 2.1 Materials

86 The combination of ground granulated blast-furnace slag and waste glass powder (GP) as

87 precursors was employed to produce the one-part alkali-activated materials (AAMs), and a solid

88 sodium silicate anhydrous powder and APC residues were used as activators. The Na_2SiO_3-

89 anhydrous powder with 35.8% Na_2O and 62.9% SiO_2 content by weight was procured from China.

90 The APC residues was collected from a local sewage sludge incinerator which burns about 1200

91 tonnes of dewatered sewage sludge by fluidised bed furnaces (Sludge Treatment Facilities, T-park,

92 Hong Kong) [12] and the waste glass was collected from a local beverage bottle recycler. The APC

93 residues and waste glass were dried in an oven at 105 °C for 48 hours and then ground separately

94 in a ball mill for 2 hours and 90 min. The mineral compositions and particle size distributions of

95 the raw materials are shown in Fig.1. Referring to XRD, the waste GP and slag showed an

96 amorphous hump, while crystalline Na_2SO_4 and NaCl were found in the APC residues. The oxide

97 compositions (determined by the XRF) of APC residues, waste GP, and slag are shown in Table 1.

98 From Table 1, the waste GP and APC residues contained a lower amount of calcium and aluminium

99 and higher amount of sodium when compared with that of the slag. The high sodium sulphate

100 content in the APC residues was resulted from that the removal of gaseous SO_2 accomplished by

101 using sodium bicarbonate in the flue gas treatment process. Besides, the amount of 4.11 wt.% Cl

102 and 5.12% of Fe_2O_3 in the APC residues was attributed to the use of seawater in toilet flushing and

103   the use of FeCl$_3$ in the chemically enhanced primary treatment process at the sewage treatment
104   plants in Hong Kong.
105   The aggregate used for preparing the mortars was a river quartz sand sourced from China. The
106   particle size distribution of the sand is shown in Fig. 2 and the fineness modulus of the river sand
107   was 2.1.
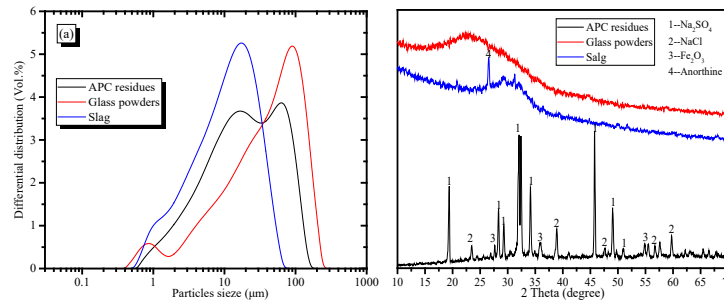
109   Fig.1 Particles size distribution and XRD pattern of raw materials

111   Table 1 Chemical compositions of materials used

	Na$_2$O	MgO	Al$_2$O$_3$	SiO$_2$	P$_2$O$_5$	SO$_3$	Cl	K$_2$O	CaO	Fe$_2$O$_3$	Others
Slag	-	7.44	16.4	34.0	0.14	2.18	0.04	0.65	36.6	0.52	2.03
GP	15.1	1.38	2.17	68.7	0.12	0.18	0.03	0.76	10.8	0.40	0.36
APC residues	35.1	1.83	4.64	7.56	3.52	33.0	4.11	0.67	3.78	5.12	2.48
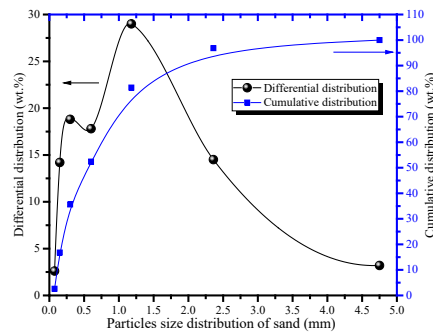
114   Fig.2 Particle size distribution of river quartz sand

115   2.2   Sample preparation
116   The one-part alkali-activated paste and mortar were produced by just adding water into the pre-
117   mixed dry precursors and solid activators. The alkali-activated mortar was prepared with a fixed
118   water/precursor ratio of 0.3 and a sand/binder ratio of 1.0. Usually, the equivalent Na$_2$O or the mass
119   ratio of alkali/precursors was used to determine the content of activator in AAMs. In this study, the

hybrid activator was prepared by mixing the APC residues and the commercially sourced sodium silicate with mass ratios of 0:1, 1:1, and 2:1, and the content of sodium silicate/precursors was set as 10%. The mix proportion of the one-part alkali-activated mortar are shown in Table 2. The two precursor powders, hybrid activators and the rive quartz sand were firstly mixed for 3 min in a mechanical mixer, and then the water were directly added into the dry powders to mix for the other 3 min. The fresh alkali-activated paste and mortar were cast into moulds and vibrated to reduce air bubbles. The alkali-activated mortars were cast into 40 mm×40mm×40 mm plastic moulds for the compressive strength test and 25 mm×25 mm×285 mm steel moulds for the drying shrinkage determination. The same water/precursors ratio but without the river sand was used to prepare the alkali-activated paste for the microstructure tests. All the specimens were transferred into a curing room (25°C and RH 95%) for curing. After one day, these specimens were demoulded and cured in same curing room until the test ages.

Table 2 Mixing proportions of alkali-activated mortars

NO.	Precursors	Activator (APC residues:Na_2SiO_3)	Water /Precursors	Sand /Precursors
S100-A0		0:1		
S100-A1	100% slag	1:1		
S100-A2		2:1		
S70G30-A0		0:1		
S70G30-A1	70% slag + 30% GP	1:1	0.3	1
S70G30-A2		2:1		
S50G50-A0		0:1		
S50G50-A1	50% slag + 50% GP	1:1		
S50G50-A2		2:1		

2.3   Experimental methods

2.3.1   Flowability and compressive strength

The workability of the alkali-activated mortar were assessed by a slump flow test using a truncated conical mould in compliance with the ASTM C1437 [26]. The truncated conical mould (top diameter=70 mm, bottom diameter=100 mm, height=60 mm) was filled with the one-part AAMs mortar. After 1 min, the mould was lifted vertically, and the self-flow diameter of the AAMs mortar was recorded along with two perpendicular directions. After the 25 vibrations, the slump-flow diameter of the AAM mortar was recorded. The compressive strength of AAMs mortar was

143 conducted by a hydraulic compressive machine with a loading rate of 0.6 MPa/s following ASTM

144 C 109 [27].

145 2.3.2   Drying shrinkage

146   The drying shrinkage of the AAMs was tested according to the ASTM C596 [28]. After

147 demoulded, the specimens were first immersed in 25°C water for 2 days. The initial length of the

148 specimens was recorded by the comparator and then moved into a chamber with 25±2 °C and

149 relative humidity of 50%. The specimens' length changes and mass loss were continuously recorded

150 for 3 months.

151 2.3.3   Isothermal calorimetry

152   The rate of heat evolution of AAMs during the first 80 h after casting was monitored using an

153 isothermal calorimeter (TAM Air I-Cal 4000) at 25 °C. The alkali-activated pastes with a

154 water/precursor ratio of 0.3 were mixed, and an amount of 15±0.1g paste was placed in the

155 isothermal calorimeter.

156 2.3.4   X-ray diffraction (XRD)

157   In order to follow the evolution of hydration products of the AAMs, the XRD measurements

158 were conducted. The dried fragments of AAMs were crushed and ground until passing a sieve of

159 45 μm. The AAM powders were scanned from 5° to 70° at a in step width of 0.02° using XRD test

160 (Rigaku SmartLab 9 kW-Advance).

161 2.3.5   Solid-state MAS-NMR

162   The solid-state MAS-NMR spectra (Bruker AV 400 spectrometer) were acquired at 9.4T

163 magnet and a resonance frequency of 104.3 MHz for ^{27}Al and 79.5 MHz for ^{29}Si. The ^{27}Al spectra

164 was recoded using 4.0 mm probe with zirconia rotors spinning rate of 14 kHz, a 4 μs excitation

165 pulse, a 5 s relaxation delay and a minimum of 7000 scans. The ^{29}Si spectra was recoded using 6.0

166 mm probe with zirconia rotors spinning rate of 6.8 kHz, a 0.75 μs excitation pulse, an 8 s relaxation

167 delay and a minimum of 3000 scans. The tetramethylsilane and $KAl(SO_4)_2$ were used as ^{29}Si and

168 ^{27}Al chemical shift reference standards, respectively. The Gaussian method was used to

169 deconvolute the ^{29}Si MAS NMR spectra. The ^{27}Al MAS NMR spectra were simulated by the Czjzek

170 Gaussian model to obtain a reasonable fit to the data.

171 2.3.6   SEM/EDS

172   After the compression test, small fragments from the central part of the pastes were soaked in

173 ethyl alcohol to stop the reaction and then dried at 40°C for a week in a vacuum oven. Afterward,

174 these dried fragments were used for SEM examination. The gold-coated fragments were observed

175 using an SEM (TESCAN VEGA3) with an energy-dispersive X-ray spectroscopy detector.

176 2.3.7   Toxicity characteristic leaching procedure for heavy metals

The Toxicity Characteristic Leaching Procedure (TCLP) was conducted in accordance with the USEPA Method 1311. The AAMs samples at 28 days were crushed and sieved with the size of 2 mm-3 mm sieve. The particles about 1 ± 0.1g were mixed with a glacial acetic acid (pH=2.88) at the liquid/solid ratio of 20:1. The AAM samples were tumbled in polypropylene bottles for 18 ± 2 h at 30 ± 2 rpm, and then the leaching solutions were filtrated through $0.45\mu m$ membrane filters. The solutions were digested with concentrated nitric acid and then diluted with 5% nitric acid. The concentration of heavy metals was tested using an inductively coupled plasma/optical emission spectroscopy (ICP-OES, FMX36, SPECTROBLUE).

3.   Results and discussion

3.1 Flowability

Fig.3 shows the effect of the APC residues on the flowability of the AAM mortar. Without the use of GP, the slump-flow and self-flow of the alkali-activated slag decreased with the increase of the APC residues. A reduction of the slump-flow and self-flow of 14% were resulted when 20% APC residues were added into the alkali-activated slag. For the alkali-activated slag/GP, the slump-flow and self-flow were reduced by 11%~14% and 16%~18% after the addition of 20% APC residues. The slump-flow and self-flow reduction can be explained by the irregular morphology of the APC residue particles. Incorporation of GP could increase the slump-flow and self-flow of the AAMs, indicating an improvement of the flowability. An increase of 10% and 23% of the self-flow and 13% and 24% of the slump-flow can be seen when 30% and 50% GP are added into the alkali-activated slag. The intrinsically smooth surface and non-absorbent nature of GP meant more free water was available for inter-particle lubrication [29, 30]. In addition, for the freshly AAMs mortar prepared without the APC residues, the dissolution of silicate and aluminum units from the precursors was slow. Only the Van der Waals force dominated which was easily broken by the vibration motion of the testing equipment and gave rise to a higher relative flow value. When the APC residues were added, a lower relative slump value was recorded, indicating that the fresh AAMs mortar became sticky. The sodium ions with a strong polarization effect could be associated with nonbridging oxygens that tended to form silica-rich gels or alkali rich gels, which had been reported in the soda-lime-silica glass [31]. The rich sodium ions from the APC residues accelerated the Si-O bond breakage from the precursor, and so the higher concentration of silicate units resulted in a rapid gelation reaction when the APC residues was added. The stronger bonding of initial gels increased the cohesiveness and reduced the relative flow value of the fresh AAMs mortar. From the above analysis, the inferior flowability of AAMs prepared with the APC residues can be compensated by the incorporation of GP.
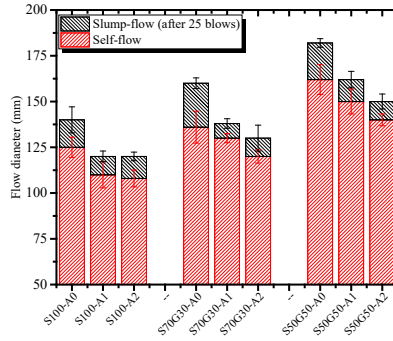
Fig.3 Effect of APC residues on the fluidity of alkali-activated materials

3.2 Compressive strength

The effect of APC residues on the compressive strength of AAMs mortar is shown in Fig.4. The compressive strength increased with the increase of curing period, but the compressive strength of S100-A0 and S70G30-A0 slightly decreased after 28 days, which was similar to those reported in previous studies [25, 32, 33]. The reason for the reduction may be attributed to the formation of the microcracks in AAMs, which were observed by scanning electron microscopy. The compressive strength of AAMs mortar decreased with increase of the APC residues and GP due to their lower reactivity than that of slag. In the presence of the APC residues, the AAMs exhibited a lower compressive strength, especially the early compressive strength. The compressive strength of S100-A0, S70G30-A0 and S50G50-A0 mortar at 1 day was decreased by 28.3%, 50.7% and 66.4% when 20% APC residues were added. A pronounced reduction of early compressive strength was linked to the retardation effect of Na_2SO_4 from the APC residues on the early reaction of AAMs. However, almost the same compressive strength of alkali-activated slag/GP at 56 days can be achieved when 10% APC residues was used. The stable growth of the compressive strength of the AAMs mortar with the APC residues could be accounted for the greater contribution of lower reaction heat and shrinkage microcracks. The lower reaction heat of the AAMs prepared with the APC residues reduced the thermal stress and formation of shrinkage microcracks, and the resulting compact structure contributed to the development of the compressive strength. It was showed that the contribution of APC residues on the early strength improvement was smaller, but more comparable compressive strength was seen in AAMs mortar with addition of the APC residues after 28 days. At 56 days, a comparable strength development of the AAMs mortars prepared with 10% and 20% APC residue to that of the control samples revealed that a certain amount APC residues and sodium silicate as hybrids activator was needed for obtaining a desired later compressive strength.
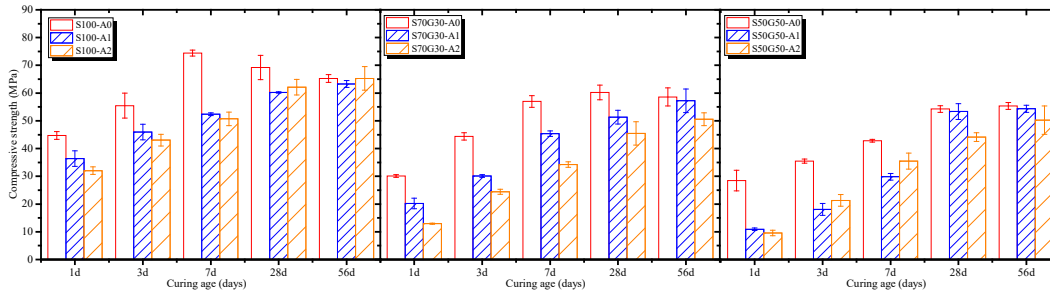
Fig.4 Effect of APC residues on the compressive strength of alkali-activated materials

3.3 Drying shrinkage

Fig.5 shows the time-dependent length and mass changes of the AAMs prepared with and without the APC residues. The drying shrinkage of all the specimens undergoes a sharper increase before 20 days, which corresponds to the sharp loss of moisture, and S100-A0 showed the highest drying shrinkage (about 8000 microstrain). The same drying shrinkage magnitude of AAMs were observed when 30% GP was used, but incorporation of 50% glass powder decreased the drying shrinkage, suggesting that increasing the GP content beyond a certain level might restrain the drying shrinkage. A reduction of 30.8% of the drying shrinkage at 90 days were seen when 20% APC residues was added into the alkali-activated slag (S100-A0). When 20% APC residues was used, a reduction of 41.9% and 51.8% of the drying shrinkage at 90 days were seen in the alkali-activated slag/GP mortar (S70G30-A0 and S50G50-A0). The lowest drying shrinkage was about 3100 microstrain when 20% APC residues and sodium silicate were used as the hybrid activator. The results showed that incorporation of the APC residues further decreased the drying shrinkage of alkali-activated slag and slag/GP due to the formation of expandable reaction products. The rich sulfate ion from APC residue would react with the dissolved aluminum from the precursors to form expandable ettringite and compensate for the drying shrinkage. On the other hand, the inhibiting effect of the APC residues for the drying shrinkage of the AAMs was due to the residue sodium sulfate, and the transformation of anhydrous sodium sulfate to its hydrous form yields an increase in crystal volume of 315 %. In addition, rapid moisture losses occurred during the early ages of the drying process but only marginal differences in the total moisture loss were found in the AAMs. The S100-A0 and S70G30-A0 exhibited the most considerable moisture loss, approximately 4%~6% by mass, and the APC residue could slightly reduce the moisture loss of AAMs.

The drying shrinkage of cement-based materials usually occurs due to the removal of moisture. During the drying procedure, a large capillary stress would be generated to cause the shrinkage deformation, and the relation of the degree of saturation and length change in cement-based materials was linear [34]. For the AAMs, two distinct slopes in the drying shrinkage-moisture loss

curve were observed. A steeper slope was found when the moisture loss was more than 5%, meaning that the drying shrinkage dramatically increased per unit moisture loss at the later ages of drying, which was consistent with the previous studies [24, 35]. The AAMs would re-absorb moisture from the environment to achieve a re-saturation of partly gels pore and a drying shrinkage deformation could be partly restored after soaking the specimens for 3 hours in water. From Fig.4, after soaking, 85% drying shrinkage was irreversible for the alkali-activated slag (S100-A0), and 73% and 75% irreversible drying shrinkage were observed when the 30% and 50% GP were used (S70G30-A0 and S50G50-A0). The result illustrated that the incorporation of GP slightly decreased the re-absorption potential of moisture of the alkali-activated slag and reduced the magnitude of the irreversible shrinkage induced by drying. In addition, the re-absorption potential of the alkali-activated slag and slag/GP increased with the increase of APC residues, illustrated that the APC residues reduced the irreversible shrinkage. Approximately 45%~65% drying shrinkage in the alkali-activated slag and slag/GP was irreversible when the APC residues was added, and the lowest drying shrinkage and irreversible shrinkage were found in S50G50-A2. Fig.6 showed the appearance of the AAMs. From Fig.6, many visible macrocracks occurred on the surface of the alkali-activated slag (S100-A0) and the obvious bending deformation were found of the sample without the APC residues alkali-activated slag/GP (S70G30-A0), while the other specimens with the APC residues and GP remained intact shape.

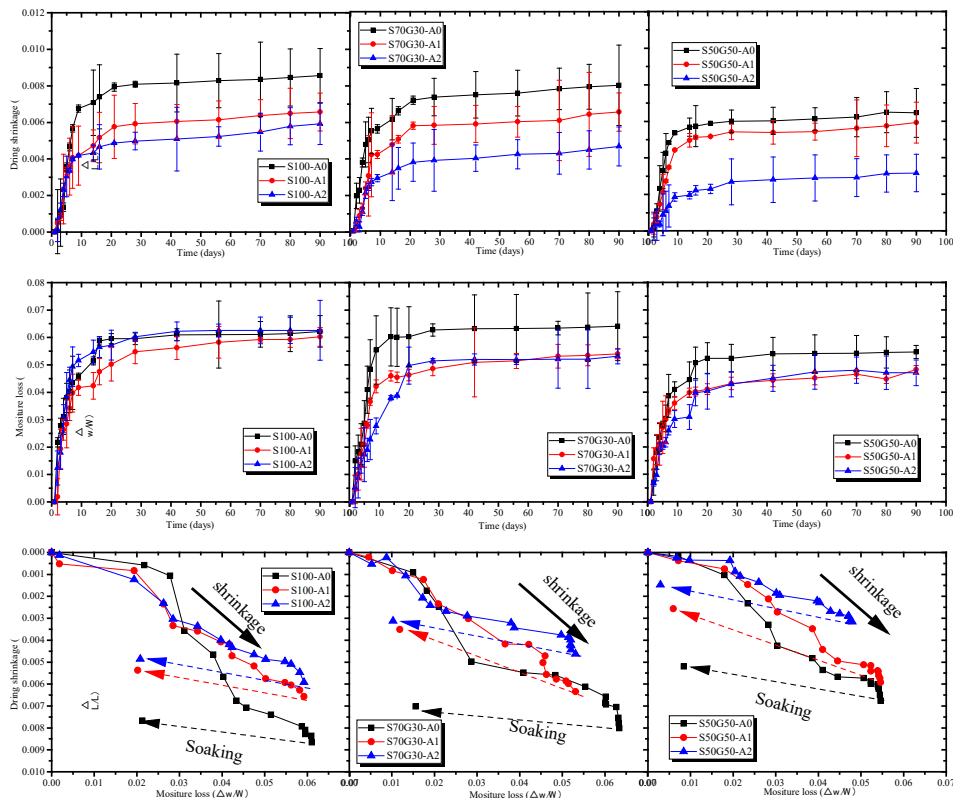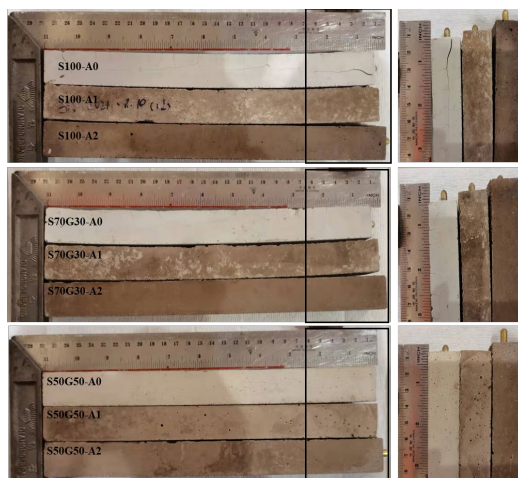Fig.5 Drying shrinkage and moisture loss of AAMs


Fig.6 Appearance of AAMs specimens after 90 days

Ye et al., [36, 37] reported that the capillary pressure induced by loss of interlayer moisture drove the gels particles closer and a reduction of interlayer spacing of C-(N)-A-S-H gels, which lead to a microstructural rearrangement and reorganization of C-(N)-A-S-H gels during the drying process. After soaking, the C-(N)-A-S-H gels original structure would fail to be rebuilt once the microstructural rearrangement and reorganization occurred, namely the irreversible shrinkage. Therefore, the lower drying shrinkage and irreversible shrinkage of AAMs with APC residues and GP was closely related to the structure and type of reaction products. Because of the GP and APC residues with a lower content of aluminum and calcium, the lower drying shrinkage and irreversible shrinkage of AAMs was attributed to the reduction of the C-(N)-A-S-H gels content due to the lower dissolution of aluminum and calcium from the precursors [33, 38]. The more alkali cations from the APC residues and GP could be incorporated into the chains of the aluminosilicate structure or absorbed on the surface to balance the charges, which improved the stacking regularity of C-(N)-A-S-H gels, and the gels easily occurred the rearrangement and reorganization. In addition, the dissolution of silicate from the soda-lime-silica glass powder was preferred to the formation of sodium silicate gels (N-S-H) with a higher sorption property in alkali solution, which resulted in a lower the irreversible shrinkage in alkali-activated slag/GP.

3.4 XRD

Fig.7 and Fig.8 illustrates the effect of APC residues and glass powders on the XRD pattern of the AAMs after 3-days and 28-days. At 3-days, the XRD patterns of alkali-activated slag and slag/GP were dominated by a broad scattering characteristic of its amorphous nature and a small amount of hydrotalcite. In addition, the remnant anorthite from unreacted slag was identified,

implying its strong stability in strong alkali solutions. For S100-A0 samples, a broad hump feature at about 29° was exhibited corresponding to the low crystallinity of C-(N)-A-S-H gels. With increase of the GP content, some crystalline peak (11.3° and 21.2°) disappeared or decreased, and this could be attributed to that the amorphous silica species from the GP increased the more difficult transition of the amorphous gel to crystalline materials, which was consistent well with a previous study [39]. When the APC residues was used, a new crystalline phase of ettringite and Friedel's salts as secondary reaction products were found in the alkali-activated slag and slag/GP. The result showed that the sulfate and chloride ions from the APC residues reacted with the aluminum phase dissolution to form the ettringite and Friedel's, which could result in crystallization stress to reduce the drying shrinkage of the alkali-activated materials as shown in Fig.5. However, the formation of ettringite was governed by the alkalinity and molar ratio of $[CaO][SO_3]/[Al_2O_3]$ in the pore solution. With increase of GP, the limited content of $[Al_2O_3]$ from slag could be rapidly exhausted by forming poorly crystalline AFm or hydrotalcite phases. Therefore, these minor crystalline phases were not identified by the XRD in the S50G50-A2 and S50G50-A4 samples and the similar results were reported in a previous study [40]. From Fig.8, the same peaks at 28days, were found in these AAMs samples, implying no new reaction products were formed, but the lower intensity of Na_2SO_4 peak illustrated that smaller sulphate from the APC residues was consumed.
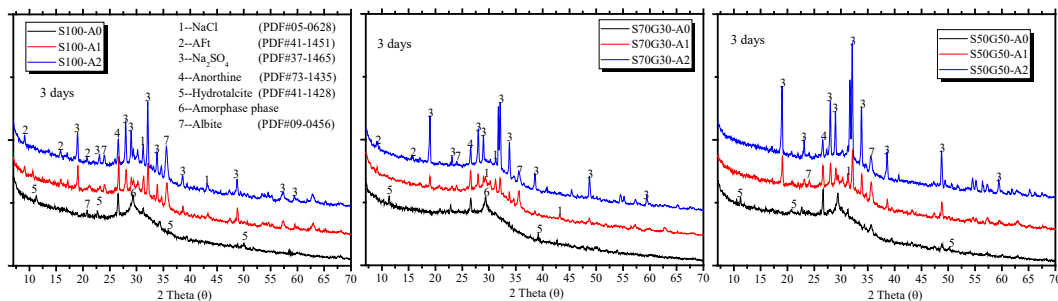
Fig.7 Effects of the APC residues on the XRD pattern of alkali-activated materials at 3 days
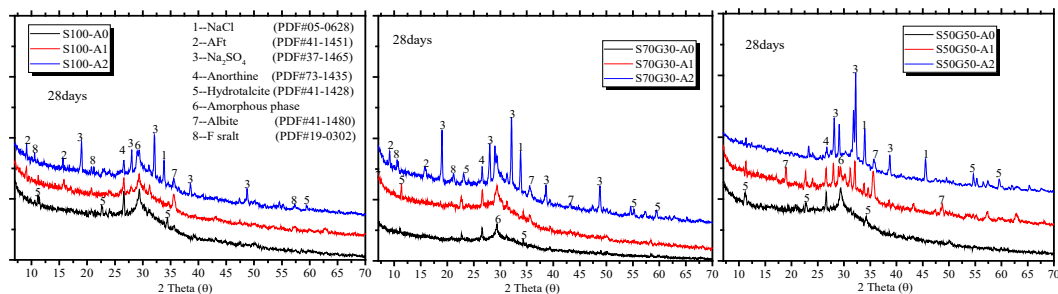
Fig.8 Effects of the APC residues on the XRD pattern of alkali-activated materials at 28 days

3.5 Reaction heat

333   The heat flow of the one-part alkali-activated materials is illustrated in Fig.9. Two exothermic
334   peaks can be observed for the alkali-activated slag (S100-A0) and slag/GP (S70A30-A0 and
335   S50G50-A0). A long induction period varying from 6 h to 10 h between the first and second peak
336   (peak I and II) was found in AAMs without the APC residues. The initial exothermic peak occurred
337   after mixing with water due to the wetting and dissolution of the precursor and solid alkali, and the
338   second peak was attributed to the formation and precipitation of initial gels. These initial gels
339   phases on the surface of unreacted precursors as protective layer can inhibit the further alkali
340   activation reaction, which resulted in induction period. The main reaction product in alkali-
341   activated slag was a mixed crosslinked/non-crosslinked C-(N)-A-S-H gels, while the addition of
342   N-S-H gels was found in the alkali-activated slag/glass [33, 41]. When the APC residues was used,
343   three exothermic peaks were observed in AAMs. The initial peaks (peak I) immediately appeared
344   just after the addition of the water, followed by a short induction period, second peak (peak II)
345   between about 2.5 h and 10 h, a dormant period between about 5 h-15 h and another small
346   exothermic peak (peak III). The AAMs paste with a rapid reaction gave a high second reaction peak
347   (Peak II) and the intensity of peak II of AAMs decreased with the increase of the APC residues.
348   The APC residues shortened the induction period between the peaks I and II. The reason was mainly
349   that the alkali metal ions from the APC residues accelerated the dissolution of the precursors due
350   to its strong polarization effect and increased the concentration of aluminum and silicon units in
351   the pore solution. The acceleration of the alkali metal ions from APC residues contributed to a rapid
352   reaction process, which reduced the flowability of AAMs, as shown in Fig.3. These precipitation
353   of initial gels products on the surface of the precursor retarded the further alkali activation reaction,
354   so the longer dormant periods with low heat evolution period between peaks II and III were found
355   in the AAMs with APC residues. During this stage, the sulfate of the APC residues could steady-
356   state diffuse and gradually react to form ettringite, corresponding to peak III. In addition, the rate
357   of heat release in the induction period decreased with the increase of the APC residues. The sodium
358   sulfate (Na_2SO_4) could be present in the form of sodium sulfate decahydrate ($Na_2SO_4 \cdot 10H_2O$) in
359   water, so the $Na_2SO_4 \cdot 10H_2O$ could serve as an endothermic agent to absorbed the heat generated
360   from the alkali reaction and decomposed to yield anhydrous sodium sulfate and a saturated solution
361   of Na_2SO_4 [15].
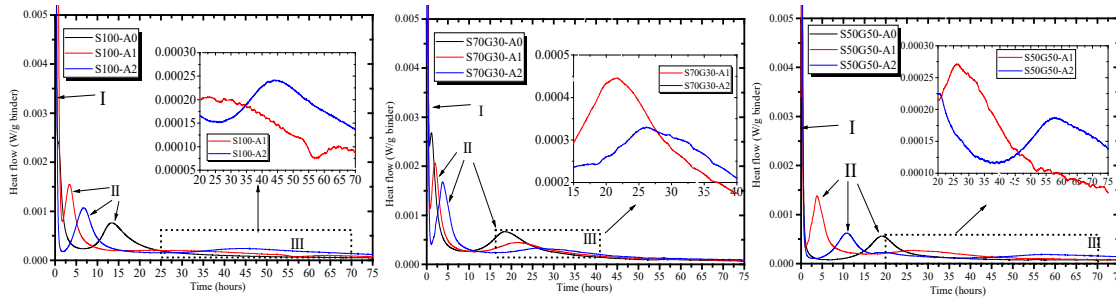
Fig.9 Effects of APC residues on the heat flow of the alkali-activated materials
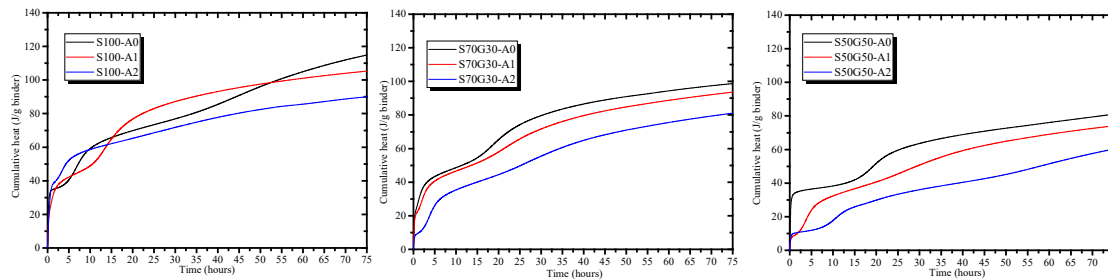
The effect of APC residue on the cumulative heat of the alkali-activated materials are illustrated in Fig.10. From Fig.10, the total cumulative heat of the AAMs paste decreased with the replacement of slag by the lower activity APC residues and GP. As shown in Table1, the AAMs gradually transformed into a low calcium system with the increase of GP and APC residues, and fewer calcium ions were available from the slag resulting in a slower reaction [42, 43]. Besides, the reason can be attributed to the retarding effect of a high concentration of sodium chloride in the system. A high level of sodium chloride had been found to almost stop the reaction of the alkali-activated slag in previous studies [44, 45].

Fig.10 Effects of APC residues on cumulative heat of the alkali-activated materials

In the Na_2SO_4-activiated slag, the sulfate would react with the Ca and Al released from the hydrolysis of slag to produce the gypsum, ettringite or layered double hydroxides (hydrotalcite and AFm type). However, for construction purposes, the sole Na_2SO_4 as activator in this system was seldom used due to the low early strength. In this study, the APC residues and anhydrous sodium silicate were used as hybrid activators to produce the AAMs, and the solid alkali would first dissolve to provide a solution with high pH, which contributed to the breaking of the Ca-O, Si-O and Al-O bond of precursors. More Ca easily entered the solution than the Al and Si because of the weaker Ca-O bond, and these Ca could react with the SiO_4 and AlO_4 to form the hydrotalcite-like phases and amorphous gels with a low Ca/Si ratio. Simultaneously, the presence of more alkali cation from the APC residues accelerated the breaking of the Si-O and Al-O bond due to its strong polarization effect. The high concentration of the aluminium and silicate units gave rise to the rapid formation of small amounts of hydrotalcite and ettringite although the main products were C-A-S-

386   H gels. In addition, the residual Na_2SO_4 in the forms of the thenardite was identified by XRD, but

387   the gypsum was not observed in the AAM samples (S50G50). This indicates that the sulfate from

388   the APC residues could directly reacted with the available Ca and Al released by the hydrolysis of

389   slag to form the ettringite or hydrotalcite. Therefore, the hybrid activators of the alkaline and APC

390   residues made it possible to formulate the one-part AAMs for reducing the drying shrinkage and

391   improving of the compressive strength.

392   3.6 MAS NMR

393   3.6.1 ^{29}Si MAS NMR

394   Fig.11 depicts the effect of APC residues on the ^{29}Si MAS NMR spectra of the alkali-activated

395   materials. The chemical shift of the ^{29}Si NMR could interpret the different Si species within the

396   reaction products, and the resonances contained various contributions of $Q^n(mAl)$ ($0 \leq m \leq n \leq 4$) from

397   -60 ppm to -100 ppm with different degrees of polymerization or Al substitution [46]. From Fig.8,

398   a broad ^{29}Si NMR can be seen in the alkali-activated materials, illustrated that Si species dominated

399   the contributions with a higher degree of polymerization, which corresponded to the poorly

400   crystallinity nature of the C-(N)-A-S-H gels. After deconvolution, seven peaks of the alkali-

401   activated slag and slag/GP were obtained. The unreacted slag exhibited a resonance around -71.5

402   ppm for Q^0 sites, and the unreacted glass powder was corresponded to the resonance at around -89

403   ppm for Q^3 sites and -101 ppm for Q^4 sites, as described in our previous paper [41]. When the APC

404   residues was added, a noticeable reduction in the intensity of the Q^0, Q^3 and Q^4 resonances was

405   observed, illustrating a higher reaction degree of slag and GP.

406   The C-(N)-A-S-H gels in the alkali-activated slag was a short-range ordering structure similar

407   to the tobermorite, and the resonances at -79.0 ppm, -82.6 ppm, and -87.9 ppm were attributed to

408   the Q^1, $Q^2(1Al)$, and Q^2 sites within the silicate group of the C-(N)-A-S-H gels [47]. The silicate

409   tetrahedra of gels were chain mid-members (Q^2), and there was a strong thermodynamics

410   preference for Al substitution for Si in the gels interlayer. The Al substitution for Si resulted in

411   local distortions and reduced the stacking regularity of gels structure, which would generate excess

412   charges due to the difference of the Al and Si pairing tetrahedra. The $Q^2(1Al)$ resonances were

413   more intense in the alkali-activated slag and slag/GP when the APC residues was used, indicating

414   a higher substitution for Si in the gels interlayer. The $Q^1(I)$ and $Q^1(II)$ resonances were attributed

415   to Q^1 species charge-balanced by Ca^{2+} and Na^+/H^+ based on molecular dynamics and previous ^{29}Si

416   MAS NMR studies of alkali-activated slag [48-50]. The APC residues reduced the intensity of $Q^1(I)$

417   resonances, but the $Q^1(II)$ resonances had slightly increases, showing that the more Na^+ or H^+ shield

418   the silicate chain of the C-(N)-A-S-H gels to a greater extent than Ca^{2+}.

419   For the alkali-activated slag, two peaks were observed locating at -87 ppm and -90 ppm

420 corresponding to the $Q^3(1Al)$ and $Q^4(3Al)$ resonances. The identification of the $Q^3(1Al)$ resonances

421 indicated a significant extent of cross-linking structure within the C-(N)-A-S-H gels [48, 51]. The

422 $Q^3(1Al)$ and $Q^4(3Al)$ resonances in the alkali-activated slag exhibited a much higher intensity when

423 the APC residues were used, indicating the continuous consumption of slag and the formation of

424 the aluminum silicate structure. The $Q^4(3Al)$ resonances at -90 ppm in the alkali-activated slag/GP

425 may be attributed to the formation of the N-(C)-A-S-H gels, but these resonances were not observed

426 in the alkali-activated slag/GP because the Q^3 and Q^4 resonances contained contributions from

427 overlapping resonances from $Q^3(1Al)$ and $Q^4(3Al)$ environments of the N-(C)-A-S-H gels. The role

428 of Ca and Al in the silicates/aluminosilicates gels could displace the Na and Si, which degraded the

429 N-(C)-A-S-H gels in favour of C-(N)-A-S-H gels formation, and the N-(C)-A-S-H gels could form

430 until the available Ca was exhausted. For the alkali-activated slag/GP, the higher amount of Na

431 from GP and APC residues incorporated into C-A-S-H gels indicated that a lesser amount of Ca

432 was released from the slag, which might form N-(C)-A-S-H gels in S50G50 samples.
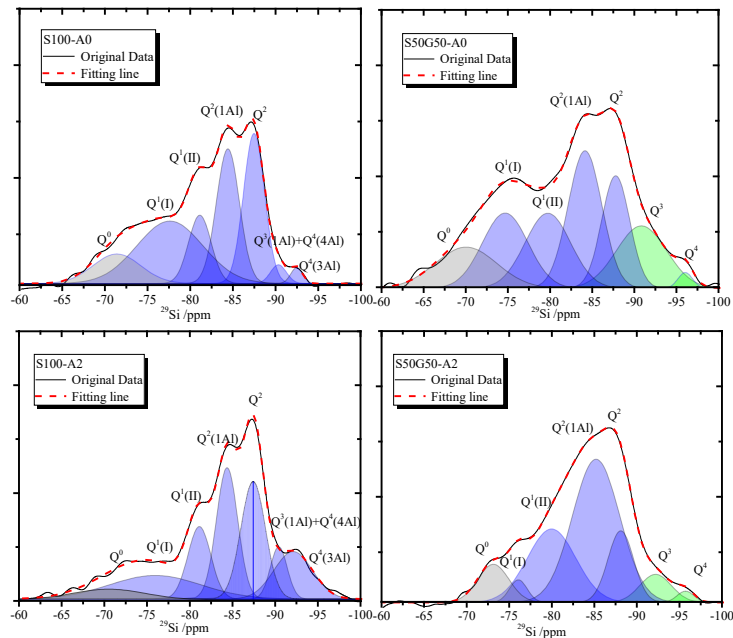
433

434   Fig. 11. ^{29}Si MAS-NMR spectra for alkali-activated materials at 28days.

435 3.6.2 ^{27}Al MAS NMR

436   Fig.12 shows the ^{27}Al MAS NMR spectra for the alkali-activated materials. All alkali-

437 activated materials exhibited a broad and asymmetrical tetrahedral Al resonance (Al^{IV}) with a low

438 intensity between 40 ppm and 90 ppm and a sharp octahedral Al resonance (Al^{VI}) between -20 ppm

439 and 40 ppm. According to the quadrupolar effect, the significantly ordered sites of Al-containing

440 crystalline phases exhibited at the chemical shift form -20 ppm to 40 ppm [50]. The broad and

441 asymmetry resonance between 40 ppm and 90 ppm denoted the presence of overlapping

442 components, and this resonance was assigned to a lower crystallinity degree and local disorder of

443 the aluminosilicate glassy fraction in the C-(N)-A-S-H gels and the remnant of the precursor. When

444 APC residues was added, a lower intensity in the first resonance but a higher intensity in the second

445 resonance were noted, indicating that the contents of poorly crystallinity gels decreased and the

446 amount of crystalline phase increased in S100-A4 and S50G50-A4. The results illustrated that the

447 APC residues contributed to the formation of Al-containing crystalline phases (e.g., the ettringite

448 and monosulfate) [52], but the glass powder might reduce the C-(N)-A-S-H gels content due to the

449 limited dissolution of Al_2O_3 and CaO from the precursors. In addition, the ^{29}Si NMR result showed

450 the presence of $Q^2(1Al)$, $Q^3(1Al)$ and $Q^4(3Al)$ in the samples, so these Al^{IV} resonance corresponded

451 to the Al $q^4(3Si)$ and Al $q^4(4Si)$.

452 Deconvolution of the ^{27}Al NMR data between 30 ppm and 90 ppm showed five different

453 tetrahedral Al sites. The distribution of Si sites in the slag was dominated by species with higher

454 Al substitution and lower polymerization, which was reported in previous studies [48, 52]. The

455 strong alkali solution increased the absorption of Na on the surface of the precursor and reacted

456 with the dissolution of the SiO_4 units. The remnant unreacted slag at 52.3 ppm was observed, and

457 the intensity of the resonance decreased with the addition of APC residues due to the accelerated

458 effect for the hydrolysis of Si-O linkages in slag. The resonance at 67.2 ppm assigned as q^3 is

459 attributed to Al in cross-linked bridging tetrahedra within the aluminosilicate chains in the C-(N)-

460 A-S-H gels. The presence of q^3 in the alkali-activated slag indicated a perturbation of the local

461 electric field gradient and a high level of aluminosilicate chain cross-linking in the gel's structure,

462 aligning with the previous studies [50, 53]. The resonance at 58.7 ppm assigned as $q^2(II)$ was

463 attributed to the bridging tetrahedra of Al, and the resonance at 74.3 ppm assigned as $q^2(I)$ was

464 attributed to the different clustering cations to balance the excess charge, which led to the local

465 distortion of Al bridging sites in C-S-H gels structure [48]. According to the thermodynamic theory,

466 the Al showed preferred substitution for Si in the tetrahedra of C-A-S-H gels, so the intensity of

467 $q^2(I)$ and $q^2(II)$ resonance could be used to describe the Al from substituting for Si in the pairing

468 tetrahedra in the C-A-S-H gels structure. The resonance $q^2(I)$ in the alkali-activated slag was

469 slightly lower than that of the sample with the addition of the APC residues, suggesting more Al

470 bridging site charge-balanced by Na^+ instead of Ca^{2+} due to its lower electron density than calcium

471 [54]. A similar trend was obtained in the alkali-activated slag/glass powder when the APC residues

472 was used. The $q^2(II)$ resonance of the alkali-activated slag/GP increased with the addition of the

473 APC residues, illustrating the formation of more bridging tetrahedra of Al and less disorder of the

474 C-(N)-A-S-H gels chain.

475   A single Al^V resonance at 38.5 ppm were identified in the ^{27}Al NMR spectra, which was

476   attributed to the charge-balancing of C-(N)-A-S-H gels interlayers [48, 55]. The intensity of Al^V

477   resonance slightly decreased with the addition of APC residues and GP. The part of dissolved Al

478   could react with sulfate ions from the APC residues to form the AFm/AFt and hydrotalcite. The GP

479   provided a high silicate concentration and decreased the substitution of Al for Si in C-(N)-A-S-H

480   gels. These reasons led to the reduction of excess Al species in gels to balance the charge.

481   After deconvolution, three distinct tetrahedral Al sites were identified between -20 ppm~40

482   ppm. The resonance at 2.3 ppm was assigned to octahedral Al atoms in the third aluminate hydrate

483   (TAH), which were found in the alkali-activated slags [48, 52]. The resonance at 14.4 ppm (HT(I))

484   and 8.3 ppm (HT(II)) in the alkali-activated slag and slag/GP (S100-A0 and S50G50-A0) were

485   assigned to the Al in a layered double hydroxides (in AFm or hydrotalcite phase), which

486   corresponded to the Al^{VI} coordinated to OH^- and CO_3^{2-} [56]. As previously stated, the sulfate from

487   the APC residue reacted with the aluminum to form the ettringite as a secondary reaction product

488   in the alkali-activated slag, and this was consistent with the XRD results. Therefore, the two Al^{VI}

489   resonances at 12.9 ppm and 7.6 ppm in S100-A2 and S50G50-A2 were attributed to the formation

490   of the AFt and AFm/hydrotalcite with the Al octahedral coordination, which were observed in

491   Na_2SO_4-activated slags [52].
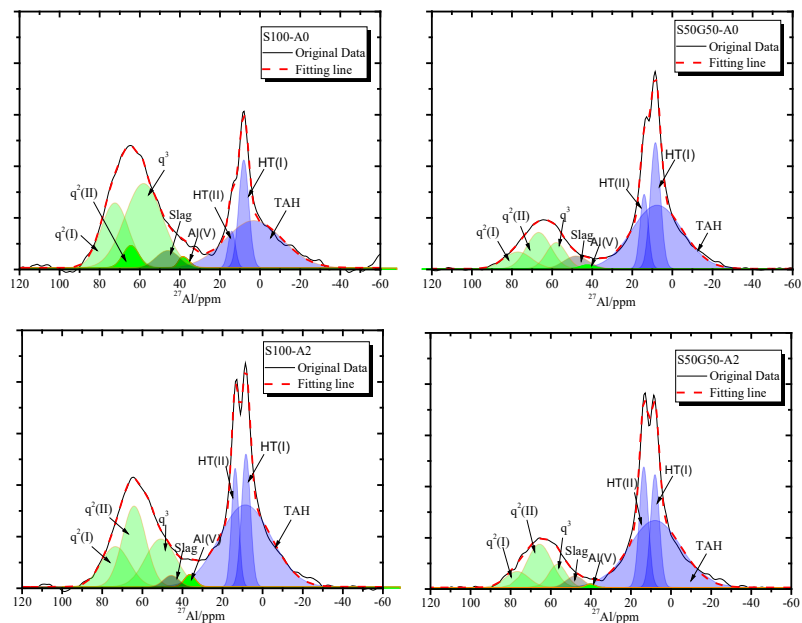
493   Fig.12. ^{27}Al MAS-NMR spectra for alkali-activated materials at 28days.

494   3.7 SEM-EDS

495   The SEM images of the alkali-activated materials at 28 days are shown in Fig.13 and the

496   element constitution of the alkali-activated materials are summarised in Table 3. The image of

497   S100-A0 showed obvious microcracks, and a smaller content of microcracks were found in

498   Fig.13(a). When the GP and APC residues was used, the residual GP particles were wrapped by a

499   continuous amorphous phase (Fig.13(c)), and the hollow and irregular of remnant Na_2SO_4 was

500   found in Fig.13(f), illustrating that the sulfate was consumed. In addition, the plate-like structures

501   were identified as the crystalline of albite ($NaAlSi_3O_8$) contained a low Ca and high Si and Al

502   content in Fig.13(c), (d) and (e), which also identified by the XRD. The microcracks in Fig.13 (a)

503   and (b) were closely related to the higher reaction heat and larger drying shrinkage. Microcracks

504   were found in the S100-A0 and S70G30-A0 (as shown in Fig.13 (a) and (b)) due to the thermal

505   stress incurred by the excessive reaction heat [57, 58]. These reaction products of the Si-rich gels

506   and Al-rich gels in the AAMs contained a higher uncombine water content, causing substantial

507   shrinkage and therefore microcracking [59]. In the presence of the APC residues, the AAMs

508   exhibited lower reaction heat and drying shrinkage resulting in less microcracking. Incorporating

509   GP would decrease the reaction heat due to their lower activity than that of slag, as discussed earlier.

510   Therefore, the reaction products of the alkali-activated slag have a dense microstructure as a result

511   of a stable development of later compressive strength was achieved when the APC residues was

512   used.
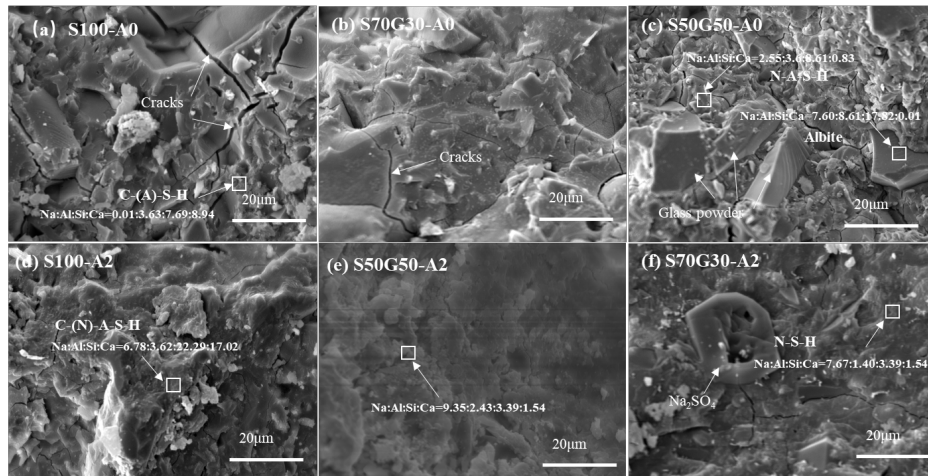
513

514   Fig.13 SEM-EDS images of alkali-activated materials at 28days

515   According to the ESD results, the element of Ca, Si, Al and Na was found in the alkali-

516   activated slag (S100-A0), illustrating that the main products were the hydrated calcium silicate (C-

517   S-H) gels containing varying levels of Al and Na. The average values of the Na/Al, Ca/Si and Al/Si

518   ratio of the gels in S100-A0 were 1.61, 1.28 and 0.39, respectively. The elementary composition of

519   gels phase had been greatly altered: a reduction of Ca/Si and Al/Si ratio, and an increase of Na/Al

520   ratio of the gels were seen with the incorporation of the APC residues. The changes of the Na/Al,

521   Ca/Si and Al/Si ratios of the C-(N)-A-S-H gels phase was attributed to the slag replaced by the

522 APC residues with rich sodium and lower calcium contents. The smaller amount of Al can be

523 incorporated into the poorly crystalline C-S-H gels to form C-A-S-H gels, meanwhile, the presence

524 of a higher amount of Na from the APC residues in the gels suggested the C-S-H gels intermixing

525 with C-(N)-A-S-H gels in which the Na cations served as negative charge balance. In addition, the

526 elemental analysis of the amorphous gels showed higher Si and Na amounts in S50G50-A2,

527 indicating the formation of the sodium silicate gels (N-S-H) with traces of Al. The formation of N-

528 S-H gels in S50G50-A2 was also a factor for increasing the reversible drying shrinkage, as

529 discussed above in Fig.5.

530 For the alkali-activated slag/GP, the Ca/Si ratio decreased, and the Na/Al and Al/Si ratios

531 increased when the APC residues was used. The decrease of the Al/Si and Ca/Si ratios was mainly

532 due to sodium from APC residues accelerated the breakage of the Si-O bond of GP and released

533 silicate units. This change in the Na/Al and Al/Si ratios contribute to the formation of a stable bond

534 for the alkali ions from the GP and APC residues, and also caused internal stresses in the local

535 microstructure, which degraded the early compressive strength of AAMs mortar [7, 37]. The higher

536 cross-linking of gels offered by the presence of Al was expected to form a stable microstructure

537 because this replacement of Si^{4+} with Al^{3+} immobilized more alkali ions [60]. Therefore, the low

538 Ca content and high Na content in the gel phases inferred the presence of N-(C)-A-S-H gels. The

539 N-(C)-A-S-H gels with a higher Al/Si was usually present in the low calcium alkali-activated

540 material system and regarded as a zeolite precursor, which was an aluminosilicate network with a

541 three-dimensional structure [48]. Due to the low crystallinity of these gels in the AAMs, it was hard

542 to be distinguished by XRD, but the coexistence of the C-(A)-S-H and N-(C)-A-S-H gels in the

543 alkali-activated materials has been reported previously [51, 61]. In addition, the sufficient levels of

544 alkali were provided with the increase of the APC residues and GP and resulted in increased

545 formation of the N-(C)-A-S-H gels. In fact, the Al and Ca in the silicates/aluminosilicates gels

546 could displace Si and Na, which degraded the N-(C)-A-S-H gels in favour of C-(A)-S-H gels

547 formation. The insufficient Ca and Al by replacing slag by GP and APC residue restrained the

548 formation of the C-(A)-S-H gels, and the N-(C)-A-S-H gels were formed in the AAMs until the

549 available Ca was exhausted. With increase of APC residues, the increase of Al/Si ratio in the gels

550 might lead to some dissolved Al from the APC residues diffused into the N-(C)-A-S-H gels'

551 structure.

552 Table 3 Average values of molar ratios of the alkali-activated materials at 28 days

S100	Na	Al	Si	Ca	Ca/Si	Na/Al	Al/Si	S100	Na	Al	Si	Ca	Ca/Si	Na/Al	Al/Si
	4.3	7.61	15.09	16.8					6.78	3.63	22.29	17.02			
A0	2.36	6.26	14.04	14.66	1.28	1.61	0.39	A2	8.31	4.01	22.81	16.51	0.76	2.0	0.22
	12.7	3.1	9.64	11.9					5.98	1.58	25.24	16.24			
	3.3	1.1	5.44	9.99					6.85	4.39	20.94	15.99			

	Na	Al	Si	Ca	Ca/Si	Na/Al	Al/Si		Na	Al	Si	Ca	Ca/Si	Na/Al	Al/Si
	0.01	3.63	7.69	8.94					6.02	8.33	16.55	15.03			
	1.43	2.57	4.84	6.4					7.5	13.49	18.57	13.61			
S70G30	Na	Al	Si	Ca	Ca/Si	Na/Al	Al/Si	**S70G30**	Na	Al	Si	Ca	Ca/Si	Na/Al	Al/Si
	9.23	5.62	16.35	13.45					6.94	9.96	10.89	6.32			
	9.22	5.61	16.33	13.43					9.35	2.43	13.52	6.25			
A0	4.16	1.55	29.23	13.22	0.70	1.92	0.27	A2	8.43	7.59	12.45	6.09	0.45	2.19	0.42
	9.54	5.91	18.16	13.02					9.15	4.62	17.68	6.0			
	10.46	5.18	18.28	12.48					6.04	1.81	15.25	5.45			
	9.64	2.4	19.99	11.98					5.45	2.67	11.47	5.31			
S50G50	Na	Al	Si	Ca	Ca/Si	Na/Al	Al/Si	**S50G50**	Na	Al	Si	Ca	Ca/Si	Na/Al	Al/Si
	4.44	4.3	9.96	2.65					5.74	1.24	3.09	2.61			
	9.08	4.23	15.64	2.63					7.67	1.4	3.39	1.54			
A0	10.09	1.43	14.31	7.35	0.36	2.78	0.32	A2	5.55	3.6	8.61	0.83	0.35	3.48	0.44
	11.88	4.41	12.45	-					17.84	8.17	12.73	1.2			
	5.26	5.41	12.75	6.27					17.89	5.02	16.2	-			
	9.23	3.06	17.51	7.15					9.9	4.02	10.16	10.1			

3.8 TCLP test

The safe disposal of the contaminated APC residues, such as immobilization of heavy metals, is an essential task of environment protection. Table 4 summarized the concentration of the heavy metals leaching from AAMs with the APC residues. From Table 4, the AAMs with the APC residues released a relatively higher concentrations of Ag, Pb and Sb, followed by Co, Cr and Zn, but the concentrations of all heavy metals were below the regulatory limits advised by the U.S. EPA. The result illustrated that the heavy metals in AAMs could be encapsulated by the physical adsorption to balance the excess negative charge and chemical immobilisation into the reaction products. Besides, the alkaline of the TCLP extraction solution increased with the increase of the APC residues, and its pH value was located between 7.78 and 9.97. The high alkaline of pore solution in the AAMs also ensured that the solubility of heavy metal was kept low.

Table 4 The TCLP results of the AAMs with APC residues at 28 days (mg/L)

	Ag	As	Ba	Cd	Co	Cr	Mn	Ni	Pb	Sb	Se	Zn
S100-A1	3.40	0.13	0.18	0.13	0.34	1.02	0.09	0.02	2.28	2.68	0.26	0.46
S100-A2	3.18	0.13	0.16	0.13	0.76	0.97	0.10	0.04	2.36	2.74	0.56	0.54
S70G30-A1	3.34	0.15	0.15	0.15	0.47	0.99	0.03	0.05	2.28	2.80	0.90	0.21
S70G30-A2	3.16	0.14	0.15	0.14	0.75	0.97	0.06	0.04	2.32	2.82	0.82	0.49
S50G50-A1	3.28	0.15	0.17	0.15	0.45	1.08	0.10	0.06	2.34	2.90	0.66	0.48
S50G50-A2	3.28	0.14	0.16	0.14	0.76	0.91	0.09	0.04	2.38	2.80	0.66	0.45
U.S. EPA Limitation	5	5	100	1	1	5	-	-	5	-	1	100

4.   Conclusions

This paper presented the results of a study on the reaction mechanisms, compressive strength, and drying shrinkage of alkali-activated materials prepared by using a hybrid of APC residues and sodium silicate as an activator. The major conclusions are listed below:

(1) The rich soluble salts of the APC residues and solid sodium silicate can be used as a hybrid activator to prepare alkali-activated materials. The APC residues reduced the flowability of AAMs mortar, but the inferior flowability could be improved by the incorporation of GP. The AAMs prepared with APC residues exhibited a lower early compressive strength, but the stable development of later compressive strength was improved due to the formation of a more compact structure.

(2) The alkali-activated slag showed the highest drying shrinkage (about 8000 microstrain), and the 85% drying shrinkage was irreversible. Incorporation of the APC residues reduced the drying shrinkage (to about 3100 microstrain) and irreversible shrinkage in the alkali-activated slag and slag/GP, which was closely related to the formation of N-S-H gels and reduction of C-(N)-A-S-H gels content.

(3) The APC residue decreased the total reaction heat of the alkali-activated slag and slag/GP and three exothermic peaks were observed. The sulfate and chloride from the APC residues could react with the aluminum from the precursors to form ettringite and Friedel's salt as secondary reaction products in the alkali-activated slag and slag/GP.

(4) With replacing of slag by the GP, the insufficient Ca and Al restrained the formation of the C-(A)-S-H gels, and the N-(C)-A-S-H gels were formed in the AAMs until the available Ca was exhausted. Upon the incorporation of the APC residue, the amorphous C-(N)-A-S-H gels were formed in addition to N-(C)-A-S-H and N-S-H gels in the alkali-activated slag/GP.

CRediT authorship contribution statement.

Keke Sun: Conceptualization, Methodology, Visualization, Writing-original draft, Writing-review & editing.

Hafiz Asad Ali: Conceptualization, Visualization, Writing-review & editing.

Dongxing XUAN: Writing-review & editing.

Jiaxing Ban: Investigation and Visualization.

Chi Sun Poon: Conceptualization, Resources, Project administration, Supervision.

References

[1] M. Juenger, F. Winnefeld, J. Provis, et al., Advances in alternative cementitious binders, Cement and Concrete Research, 41 (2011) 1232-1243.

604   [2] J. Provis, A. Palomo, C. Shi, Advances in understanding alkali-activated materials, Cement

605   and Concrete Research, 78 (2015) 110-125.

606   [3] K. Sun, X. Peng, S. Wang, et al., Design method for the mix proportion of geopolymer

607   concrete based on the paste thickness of coated aggregate, Journal of Cleaner Production, 232 (2019)

608   508-517.

609   [4] S. Aydin, B. Baradan, Effect of activator type and content on properties of alkali-activated

610   slag mortars, Composites Part B: Engineering, 57 (2014) 166-172.

611   [5] M. Mastali, P. Kinnunen, A. Dalvand, et al., Drying shrinkage in alkali-activated binders-A

612   critical review, Construction and Building Materials, 190 (2018) 533-550.

613   [6] S. Wang, X. Pu, K. Scrivener, Alkali-activated slag cement and concrete: a review of

614   properties and problems, Advances in Cement Research, 7 (1995) 93-102.

615   [7] K. Sun, X. Peng, S. Wang, et al., Effect of nano-SiO_2 on the efflorescence of an alkali-

616   activated metakaolin mortar, Construction and Building Materials, 253 (2020) 118952.

617   [8] T. Luukkonen, Z. Abdollahnejad, J. Yliniemi, et al., One-part alkali-activated materials: A

618   review, Cement and Concrete Research, 103 (2018) 21-34.

619   [9] M. Kacprzak, E. Neczaj, K. Fijalkowski, et al., Sewage sludge disposal strategies for

620   sustainable development, Environmental Research, 156 (2017) 39-46.

621   [10] M. Quina, J. Bordado, R. Ferreira, Treatment and use of air pollution control residues from

622   MSW incineration: an overview, Waste Management, 28 (2008) 2097-2121.

623   [11] D. Rani, A. Boccaccini, D. Deegan, et al., Air pollution control residues from waste

624   incineration: Current UK situation and assessment of alternative technologies, Waste Management,

625   28 (2008) 2279-2292.

626   [12] L. Swann, D. Downs, M. Waye, Waste to energy solution-the sludge treatment facility in

627   Tuen Mun, Hong Kong, Energy Procedia, 143 (2017) 500-505.

628   [13] J. Li, Q. Xue, L. Fang, et al., Characteristics and metal leachability of incinerated sewage

629   sludge ash and air pollution control residues from Hong Kong evaluated by different methods,

630   Waste Management, 64 (2017) 161-170.

631   [14] N. Cristelo, I. Garcia, J. Rivera, et al. One-part hybrid cements from fly ash and electric arc

632   furnace slag activated by sodium sulphate or sodium chloride, Journal of Building Engineering, 44

633   (2021) 103298.

634   [15] A. Rashad, Y. Bai, P. Basheer, et al., Hydration and properties of sodium sulfate activated

635   slag, Cement and Concrete Composites, 37 (2013) 20-29.

636   [16] A. Rashad, Influence of different additives on the properties of sodium sulfate activated slag,

637   Construction and Building Materials, 79 (2015) 379-389.

638 [17] A. Adesina, C. Kaze, Physico-mechanical and microstructural properties of sodium sulfate

639 activated materials: A review, Construction and Building Materials, 295 (2021) 123668.

640 [18] C. Lampris, J. Stegemann, C. Cheeseman, Chloride leaching from air pollution control

641 residues solidified using ground granulated blast furnace slag, Chemosphere, 73 (2008) 1544-1549.

642 [19] P. Ren, T. Ling, Roles of chlorine and sulphate in MSWIFA in GGBFS binder: Hydration,

643 mechanical properties and stabilization considerations, Environmental Pollution, 284 (2021)

644 117175.

645 [20] P. He, B. Zhang, S. Yang, et al., Recycling of glass cullet and glass powder in alkali-

646 activated cement: Mechanical properties and alkali-silica reaction, Waste and Biomass

647 Valorization, 11 (2020) 7159-7169.

648 [21] Y. Liu, C. Shi, Z. Zhang, et al,, An overview on the reuse of waste glasses in alkali-activated

649 materials, Resources, Conservation and Recycling, 144 (2019) 297-309.

650 [22] M. Khan, J. Kuri, P. Sarker, Sustainable use of waste glass in alkali activated materials

651 against H_2SO_4 and HCl acid attacks, Cleaner Engineering and Technology, 6 (2022) 100354.

652 [23] R. Redden, N. Neithalath, Microstructure, strength, and moisture stability of alkali activated

653 glass powder-based binders, Cement and Concrete Composites, 45 (2014) 46-56.

654 [24] R. Si, Q. Dai, S. Guo, et al., Mechanical property, nanopore structure and drying shrinkage

655 of metakaolin-based geopolymer with waste glass powder, Journal of Cleaner Production, 242

656 (2020) 118502.

657 [25] B. Zhang, P. He, C. Poon, Optimizing the use of recycled glass materials in alkali activated

658 cement (AAC) based mortars, Journal of Cleaner Production, 255 (2020) 120228.

659 [26] ASTM standard C1437, Standard test method for flow of hydraulic cement mortar, West

660 Conshohocken, PA, 2020.

661 [27] ASTM C109/C109M, Standard test method for compressive strength of hydraulic cement

662 mortars. West Conshohocken, PA, 2021.

663 [28] ASTM C596, Standard test method for drying shrinkage of mortar containing hydraulic

664 cement, West Conshohocken, PA, 2018.

665 [29] J. Monzo, J. Paya, M. Borrachero, et al., Reuse of sewage sludge ashes (SSA) in cement

666 mixtures: the effect of SSA on the workability of cement mortars, Waste Management, 23 (2003)

667 373-381.

668 [30] M. Samarakoon, P. Ranjith, V. Desilva, Effect of soda-lime glass powder on alkali-activated

669 binders: Rheology, strength and microstructure characterization, Construction and Building

670 Materials, 241 (2020) 118013.

[31] C. Huang, A. Cormack, The structure of sodium silicate glass, The Journal of Chemical Physics, 93 (1990) 8180-8186.

[32] F. Collins, J. Sanjayan, Microcracking and strength development of alkali activated slag concrete, Cement and Concrete Composites, 23 (2001) 345-352.

[33] R. Redden, N. Neithalath, Microstructure, strength, and moisture stability of alkali activated glass powder-based binders, Cement and Concrete Composites, 45 (2014) 46-56.

[34] W. Hansen, Drying shrinkage mechanisms in Portland cement paste, Journal of the American Ceramic Society, 70 (1987) 323-328.

[35] R. Thomas, D. Lezama, S. Peethamparan, On drying shrinkage in alkali-activated concrete: Improving dimensional stability by aging or heat-curing, Cement and Concrete Research, 91 (2017) 13-23.

[36] H. Ye, A. Radlinska, Shrinkage mechanisms of alkali-activated slag, Cement and Concrete Research, 88 (2016) 126-135.

[37] H. Ye, C. Cartwright, F. Rajabipour, et al., Understanding the drying shrinkage performance of alkali-activated slag mortars, Cement and Concrete Composites, 76 (2017) 13-24.

[38] W. Dong, W. Li, Z. Tao, A comprehensive review on performance of cementitious and geopolymeric concretes with recycled waste glass as powder, sand or cullet, Resources, Conservation and Recycling, 172 (2021) 105664.

[39] Z. Abdollahnejad, A. Dalvand, M. Mastali, et al., Effects of waste ground glass and lime on the crystallinity and strength of geopolymers, Magazine of Concrete Research, 71 (2019) 1218-1231.

[40] C. Ma, B. Zhao, L. Wang, et al., Clean and low-alkalinity one-part geopolymeric cement: Effects of sodium sulfate on microstructure and properties, Journal of Cleaner Production, 252 (2020) 119279.

[41] P. He, B. Zhang, J. Lu, et al., Reaction mechanisms of alkali-activated glass powder-ggbs-CAC composites, Cement and Concrete Composites, 122 (2021) 104143.

[42] X. Zhu, M. Zhang, K. Yang, et al., Setting behaviours and early-age microstructures of alkali-activated ground granulated blast furnace slag (GGBS) from different regions in China, Cement and Concrete Composites, 114 (2020) 103782.

[43] B. Gebregziabiher, R. Thomas, S. Peethamparan, Temperature and activator effect on early-age reaction kinetics of alkali-activated slag binders, Construction and Building Materials, 113 (2016) 783-793.

703 [44] A. Brougha, M. Hollowayb, J. Sykesb, et al., Sodium silicate-based alkali-activated slag
704 mortars Part II. The retarding effect of additions of sodium chloride or mali, Cement and Concrete
705 Research, 30 (2000) 1375-1379.

706 [45] A. Brough, A. Atkinson, Sodium silicate-based, alkali-activated slag mortars Part I. Strength,
707 hydration and microstructure, Cement and Concrete Research, 32 (2002) 865-879.

708 [46] G. Saoût, M. Haha, F. Winnefeld, et al., Hydration degree of alkali-activated slags: A ^{29}Si
709 NMR study, Journal of the American Ceramic Society, 94 (2011) 4541-4547.

710 [47] J. Duxson, L. Provis, G. Lukey, et al., ^{29}Si NMR study of structural ordering in
711 aluminosilicate geopolymer gels, Langmuir, 21 (2005) 3028-3036.

712 [48] B. Walkley, X. Ke, J. Provis, et al., Activator anion influences the nanostructure of alkali-
713 activated slag cements, The Journal of Physical Chemistry C, 125 (2021) 20727-20739.

714 [49] F. Bonk, J. Schneider, M. Cincotto, et al., Characterization by multinuclear high-resolution
715 NMR of hydration products in activated blast-furnace slag pastes, Journal of the American Ceramic
716 Society, 86 (2003) 1712-1719.

717 [50] R. Myers, S. Bernal, J. Gehman, et al., The role of Al in cross-linking of alkali-activated
718 slag cements, Journal of the American Ceramic Society, 98 (2015) 996-1004.

719 [51] B. Walkley, R. Nicolas, M. Sani, et al., Phase evolution of C-(N)-A-S-H/N-A-S-H gel
720 blends investigated via alkali-activation of synthetic calcium aluminosilicate precursors, Cement
721 and Concrete Research, 89 (2016) 120-135.

722 [52] N. Mobasher, S. Bernal, J. Provis, Structural evolution of an alkali sulfate activated slag
723 cement, Journal of Nuclear Materials, 468 (2016) 97-104.

724 [53] A. Fernández, F. Puertas, I. Sobrados, et al. Structure of calcium silicate hydrates formed in
725 alkaline-activated slag: influence of the type of alkaline activator. Journal of the American Ceramic
726 Society, 86(8) (2003) 1389-1394.

727 [54] P. Rejmak, J. Dolado, M. Stott, et al., ^{29}Si NMR in cement: A theoretical study on calcium
728 silicate hydrates, The Journal of Physical Chemistry C, 116 (2012) 9755-9761.

729 [55] G. Sun, J. Young, R. Kirkpatrick, The role of Al in C-S-H: NMR, XRD, and compositional
730 results for precipitated samples, Cement and Concrete Research, 36 (2006) 18-29.

731 [56] P. Sideris, F. Blanc, Z. Gan, et al., Identification of cation clustering in Mg-Al layered
732 double hydroxides using multinuclear solid state nuclear magnetic resonance spectroscopy,
733 Chemistry of Materials, 24 (2012) 2449-2461.

734 [57] Z. Li, Z. Deng, X. Guo, An analysis of the microscopic cracking mechanism of hardened
735 alkali-activated slag, Construction and Building Materials, 170 (2018) 466-484.

736   [58] S. Bernal, R. Gutierrez, A. Pedraza, et al., Effect of binder content on the performance of

737   alkali-activated slag concretes, Cement and Concrete Research, 41 (2011) 1-8.

738   [59] M. Palacios, F. Puertas, Effect of shrinkage-reducing admixtures on the properties of alkali-

739   activated slag mortars and pastes, Cement and Concrete Research, 37 (2007) 691-702.

740   [60] J. Provis, P. Duxson, G. Lukey, et al., Statistical thermodynamic model for Si/Al ordering

741   in amorphous aluminosilicates, Chemistry of Materials, 17 (2005) 2976-2986.

742   [61] I. Garcia, A. Palomo, A. Fernandez, et al., Compatibility studies between N-A-S-H and C-

743   A-S-H gels. Study in the ternary diagram $Na_2O-CaO-Al_2O_3-SiO_2-H_2O$, Cement and Concrete

744   Research, 41 (2011) 923-931.

745